Astronomy
&
Astrophysics

Multiwavelength observations of a rich galaxy cluster at *z* ~ 1

The HST/ACS colour–magnitude diagram[*]

J. S. Santos[1,2], P. Rosati[3], R. Gobat[3], C. Lidman[4], K. Dawson[5], S. Perlmutter[5], H. Böhringer[2], I. Balestra[2],
C. R. Mullis[6], R. Fassbender[2], J. Kohnert[7], G. Lamer[7], A. Rettura[8], C. Rité[3], and A. Schwope[7]

[1] INAF – Osservatorio Astronomico di Trieste, via Tiepolo 11, 34131 Trieste, Italy
    e-mail: jsantos@oats.inaf.it
[2] Max-Planck-Institut für extraterrestrische Physik, Giessenbachstraße, 85748 Garching, Germany
[3] European Southern Observatory, Karl Schwarzschild Strasse 2, Garching bei Muenchen, 85748, Germany
[4] European Southern Observatory, Alonso de Cordova 3107, Casilla 19001, Santiago, Chile
[5] E.O. Lawrence Berkeley National Laboratory, 1 Cyclotron Rd., Berkeley, CA 94720, USA
[6] Wachovia Corporation, NC6740, 100 N. Main Street, Winston-Salem, NC 27101, USA
[7] Astrophysikalisches Institut Potsdam (AIP), An der Sternwarte 16, 14482 Potsdam, Germany
[8] Department of Physics and Astronomy, Johns Hopkins University, Baltimore, MD21218, USA

ABSTRACT

Context. XMMU J1229+0151 is a rich galaxy cluster with redshift $z = 0.975$ that was serendipitously detected in X-rays within the scope of the XMM-Newton Distant Cluster Project. Both HST/ACS observations in the i_{775} and z_{850} passbands and VLT/FORS2 spectroscopy were obtained, in addition to follow-up Near-Infrared (NIR) imaging in the J- and Ks-bands with NTT/SOFI.
Aims. We investigate the photometric, structural, and spectral properties of the early-type galaxies in the high-redshift cluster XMMU J1229+0151.
Methods. Source detection and aperture photometry are performed in the optical and NIR imaging. Galaxy morphology is inspected visually and by means of Sersic profile fitting to the 21 spectroscopically confirmed cluster members in the ACS field of view. The $i_{775} - z_{850}$ colour−magnitude relation (CMR) is derived with a method based on galaxy magnitudes obtained by fitting the surface brightness of the galaxies with Sersic models. Stellar masses and formation ages of the cluster galaxies are derived by fitting the observed spectral energy distributions (SED) with models developed by Bruzual & Charlot. Star-formation histories of the early-type galaxies are constrained by analysing the stacked spectrophotometric data.
Results. The structural Sersic index n obtained by model fitting agrees with the visual morphological classification of the confirmed members, indicating a clear predominance of elliptical galaxies (15/21). The $i_{775} - z_{850}$ colour−magnitude relation of the spectroscopic members shows a very tight red-sequence with a zero point of 0.86 ± 0.04 mag, and intrinsic scatter equal to 0.039 mag. The CMR obtained with the galaxy models has similar parameters. By fitting both the spectra and SED of the early-type population, we obtain a star-formation-weighted age of 4.3 Gyr for a median galaxy stellar-mass of $7.4 \times 10^{10}\ M_\odot$. Instead of identifying a brightest cluster galaxy (BCG) unambiguously, we find three bright galaxies with a similar z_{850} magnitude, which are, in addition, the most massive cluster members, with $\sim 2 \times 10^{11}\ M_\odot$. Our results strengthen the current evidence of a lack of significant evolution in both the scatter and slope of the red-sequence out to $z \sim 1$.

Key words. galaxies: clusters: individual: XMMU J1229+0151 – galaxies: high-redshift – galaxies: evolution

1. Introduction

Distant ($z \sim 1$) galaxy clusters are unique astrophysical laboratories particularly suited to witnessing and studying galaxy formation and evolution.

Detailed studies of the properties of galaxies in large samples of high-redshift clusters are required to distinguish between the two main galaxy formation scenarios, which have been discussed for over 30 years. In the *monolithic picture* (Eggen et al. 1962; Larson 1974), massive galaxies are expected to form early from a single progenitor. In contrast, the *hierarchical scenario* (Toomre 1977; White & Rees 1978) predicts that elliptical galaxies should form later, by galaxy-galaxy mergers. The behaviour of early-type galaxies (ETGs), which are found to comprise both the most massive *and* oldest systems, is the main cause of this debate. It is now established that the star-formation histories of ellipticals are mass-dependent from both observational (Thomas et al. 2005; van der Wel et al. 2005) and theoretical studies (e.g., De Lucia et al. 2004; Menci et al. 2008), such that low-mass galaxies have more extended star-formation histories than more massive ones. This implies that the less massive galaxies have a lower formation redshift than the more massive systems, whose star-formation histories are predicted to peak at $z \sim 5$ (De Lucia et al. 2006). This scenario is commonly referred to as "*downsizing*" (Cowie et al. 1996). Supporting this picture, there is strong observational evidence for the bulk of the stars in massive ellipticals being formed already at redshift >2 (van Dokkum 2005; Holden et al. 2005).

The colour−magnitude relation (CMR, Visvanathan & Sandage 1977; Sandage & Visvanathan 1978) is a fundamental scaling relation used to assess the evolution of galaxy populations. The CMR of local clusters shows the existence of a tight so-called red-sequence (RS, Bower et al. 1992; de Propris et al. 1998; Gladders & Yee 2000; Baldry et al. 2004) formed of massive red elliptical galaxies undergoing passive evolution, and the analysis of its main parameters (zero point, scatter, and slope) provides a means of quantifying the evolution of the galaxy properties with redshift. It remains, nevertheless, unclear the degree to which the CMR is affected by age and metallicity effects.

The study of high-z samples of galaxies is also important for providing information about the modelling of physical processes in semi-analytical techniques. Semi-analytical modelling (SAM) employing AGN feedback to prevent the overproduction of blue galaxies have recently succeeded in predicting a large amount of massive old galaxies (De Lucia et al. 2006; Bower et al. 2006; Menci et al. 2006; Croton et al. 2006; Somerville et al. 2008). However, several issues remain unresolved, such as the incapacity to reproduce quantitatively both the colour-bimodality in the colour−magnitude diagram and the scatter in the red-sequence, which is overestimated by a factor 2−3 (e.g., Menci et al. 2008).

The exceptional high-resolution provided by the Advanced Camera for Surveys (ACS) onboard the Hubble Space Telescope (HST) has contributed greatly to the current knowledge of galaxy evolution in dense environments. Results for eight $z \sim 1$ clusters observed as part of the ACS intermediate redshift cluster survey (Blakeslee et al. 2003a; Mei et al. 2007; Holden et al. 2005; Mei et al. 2009, and references therein), and studies of individual distant clusters (RDCS 1252.9-2927 at $z = 1.235$: Lidman et al. 2004; Demarco et al. 2007; XMMU J2235.3-2557 at $z = 1.393$: Rosati et al. 2009; Lidman et al. 2008; XMMXCS J2215.9-1738 at $z = 1.45$, Stanford et al. 2006) illustrate the prevalence of a tight RS up to $z = 1.4$, where the CMR slope and scatter are observed to have a negligible increase with redshift.

In this paper we provide a detailed analysis of the galaxy properties in XMMU J1229+0151 (hereafter, XMM1229), an X-ray selected, optically rich and distant cluster ($z = 0.975$ corresponding to a lookback time of 7.6 Gyr). We derive accurate colour measurements from the high-resolution ACS data, and characterize the galaxy morphology by both visual inspection and the fitting of Sersic profiles. Stellar masses, ages, and star-formation histories of the cluster early-types are derived by fitting the coadded spectrophotometric data with Bruzual & Charlot (2003) templates.

The paper is organized as follows: in Sect. 2, we present the imaging and spectroscopic data, as well as the data reduction procedures. The ACS morphological analysis is introduced in Sect. 3. In Sect. 4, we derive the $i_{775} - z_{850}$ CMR, and the results from the SED fitting are presented in Sect. 5. In Sect. 6, we investigate the properties of the brightest cluster galaxies. We conclude in Sect. 7.

The cosmological parameters used throughout the paper are $H_0 = 70$ km s^{-1} Mpc^{-1}, $\Omega_\Lambda = 0.7$ and $\Omega_m = 0.3$. Filter magnitudes are presented in the AB system unless stated otherwise.

2. Observations and data reduction

2.1. XMM-Newton data

The cluster XMM1229 was initially detected in a serendipitous cluster survey of the XMM-Newton archive, the XMM-Newton Distant Cluster Project (XDCP, Böhringer et al. 2005;

Table 1. Log of the archival XMM-Newton observations of XMM1229.

| Date	Obs. Id.	Rev.	Filt./Mode	T_{exp} [ks]
(1)	(2)	(3)	(4)	(5)
2000-06-13	0126700201	0094	M/F	11.7+11.6
2000-06-14	0126700301	0094	M/F	56.4+56.1
2000-06-15	0126700601	0095	M/S	24.0+23.7
2000-06-16	0126700701	0095	M/S	17.5+17.8
2000-06-18	0126700801	0096	M/S	40.8+41.1
2001-06-13	0136550101	0277	T/S	40.1+40.1
2003-07-07	0159960101	0655	T/S	51.3+54.6
2004-06-30	0136550801	0835	T1-M2/S	14.3+47.7
2005-07-10	0136551001	1023	M/S	26.9+26.7
2007-01-12	0414190101	1299	M/S	57.3+55.5
2007-06-25	0414190301	1381	M/S	26.8+26.2

Fassbender 2008). Our target was observed in 25 XMM-Newton pointings of the bright radio loud quasar 3C 273 at an off-axis angle of approximately 13 arcmin. We selected only observations whose exposure time, after cleaning for high background periods, was longer than 10 ks. Unfortunately, XMM1229 was not observed by the EPIC-pn camera, since the pn was always operated in Small Window Mode (except for Obs_Id=0126700201, which had a clean exposure time of only ∼6 ks). Therefore, we used only the data from the two XMM/MOS CCDs. The 11 observations selected for our analysis are listed in Table 1. The information given is the following: observation date (Col. 1), XMM-Newton observation identification number (Col. 2) and revolution (Col. 3), filter (M = medium, T = thin) and mode (F = full window, S = small window) used (Col. 4), good exposure time of XMM/MOS1+MOS2, after cleaning for high particle-background periods (Col. 5).

Data were processed using the XMM-Newton Science Analysis Software (SAS v7.0.0). Light curves for pattern = 0 events in the 10−15 keV band were produced to search for periods of background flaring, which were selected and removed by applying a 3σ clipping algorithm. Light curves in the 0.3−10 keV band were visually inspected to remove residual soft-proton induced flares. We selected events with patterns between 0 to 12 (single, double, and quadruple) and further removed events of low spectral quality (i.e. FLAG = 0). We obtained total exposure times of ∼370 and ∼400 ks for the XMM/MOS1 and XMM/MOS2, respectively.

The spectra of the cluster were extracted from a circular region of radius 30 arcsec centred on RA = 12:29:29.2, Dec = +01:51:26.4. The background was estimated from a circular region on the same chip of radius ∼2 arcmin centred on RA = 12:29:21.2, Dec = +01:51:55.4, after removing cluster and point sources.

We corrected vignetting effects using the SAS task EVIGWEIGHT (Arnaud et al. 2001) to calculate the emission-weighted effective area, by assigning a weight to each photon equal to the ratio of the effective area at the photon position relative to the on-axis effective area. Redistribution matrices were generated using the SAS task RMFGEN for each pointing, filter, and detector.

Time-averaged spectra for the source and background were obtained by adding the counts in each channel. Since different filters were used for the observations, we weighted each instrument effective area (ARF) and redistribution matrix (RMF) by the exposure time of the observation. Before applying the χ^2 minimization in the spectral fitting, we binned the spectra with a minimum number of 20 counts per bin.
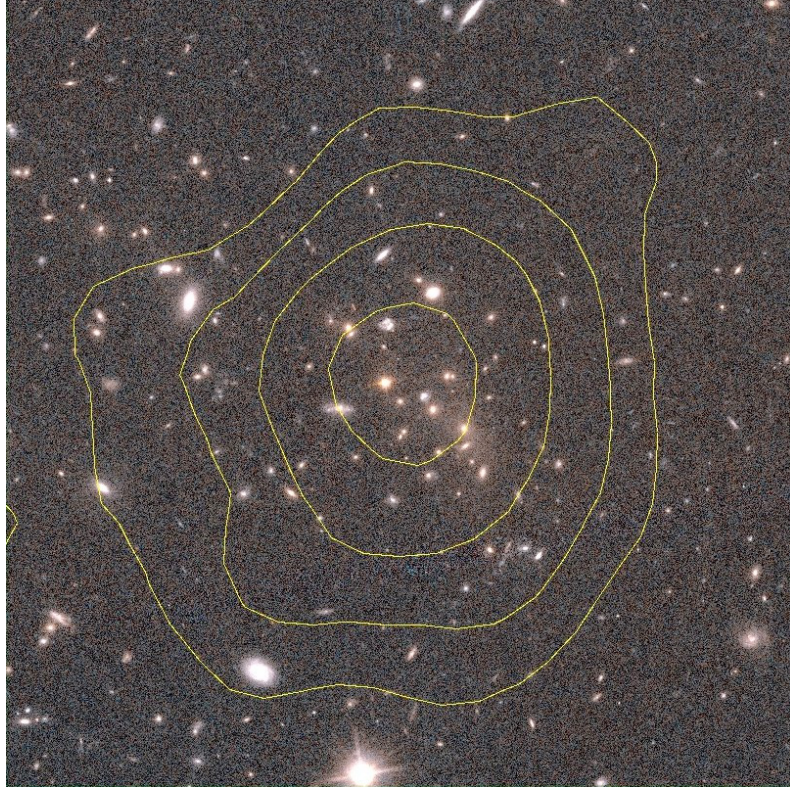
Fig. 1. HST/ACS colour image of XMMU J1229+0151 with X-ray contours. The image is centred on the cluster X-ray emission and has a size of 1.5 arcmin^2.

2.1.1. Spectral analysis

The two XMM/MOS spectra were analysed with XSPEC v11.3.1 (Arnaud 1996) and were fitted with a single-temperature `mekal` model (Kaastra 1992; Liedahl et al. 1995). We modeled Galactic absorption with `tbabs` (Wilms et al. 2000). We always refer to the values of solar abundances as presented in Anders & Grevesse (1989).

The fits were performed over the 0.5−6 keV band. We excluded energies below 0.5 keV, due to calibration uncertainties, and above 6 keV, where the background started to dominate. Furthermore, because of the relatively low S/N of the observations, we notice that instrumental Kα emission lines[1] from Al (at ~1.5 keV) and Si (at ~1.7 keV) may affect the spectral analysis significantly. Therefore, we also excluded photons in the energy range 1.4−1.8 keV from our spectral analysis. In the selected energy bands we had a total of ~1300 and ~1200 net counts for the XMM/MOS1 and XMM/MOS2, respectively.

The free parameters in our spectral fits were temperature, metallicity, redshift, and normalization, although we also performed the fit by freezing the redshift to 0.975, the median spectroscopic redshift of the confirmed member galaxies. Local absorption was fixed to the Galactic neutral-hydrogen columndensity, as obtained from radio data (Dickey & Lockman 1990).

The results of the spectral analysis are listed in Table 2, the quoted errors being of the 1-σ confidence level. The information provided is the following: detector used, (Col. 1), temperature (Col. 2), iron abundance (Col. 3), redshift (Col. 4), χ^2 and
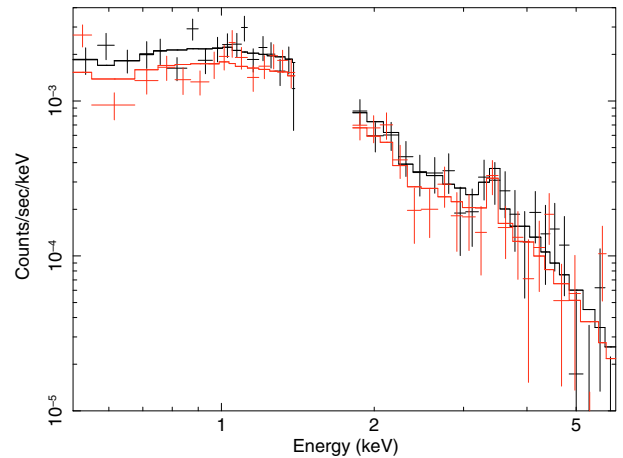
Fig. 2. X-ray spectra of XMM1229 from the XMM/MOS1 (black) and XMM/MOS2 (red) detectors. The solid lines show the best-fit models. The Fe K-line is prominent at 3.2 keV.

number of degrees of freedom (Col. 5). The last line of the table refers to the spectral fit with the redshift set to 0.975.

The rest-frame luminosity corrected for Galactic absorption in the 0.5−2.0 keV range is $(1.3 \pm 0.2) \times 10^{44}$ erg s^{-1}, for an aperture of 30 arcsec radius, which corresponds to a physical size of 240 kpc. To obtain the total cluster luminosity, we extrapolated the measured aperture luminosity to a radius of 2 Mpc, assuming an isothermal β-model (Cavaliere & Fusco-Femiano 1976), a well-known analytical formula that depends on a slope β and a core radius r_c, which closely describes the surface brightness profile of regular clusters. Unfortunately, the signal-to-noise ratio of our data was insufficient for fitting a β-model, and

---

[1] http://xmm.vilspa.esa.es/external/xmm_user_support/documentation/uhb/node35.html

Table 2. Results of the X-ray spectral analysis.

Detector (1)	kT [keV] (2)	Z_{Fe} [$Z_\odot$] (3)	z (4)	χ^2/d.o.f. (5)
MOS1	$6.2^{+1.0}_{-0.8}$	$0.37^{+0.20}_{-0.18}$	$0.96^{+0.02}_{-0.03}$	45.1/51
MOS2	$6.2^{+1.1}_{-0.6}$	$0.42^{+0.22}_{-0.21}$	$0.95^{+0.03}_{-0.02}$	50.1/44
MOS1+2	$6.25^{+0.69}_{-0.55}$	0.38 ± 0.14	0.96 ± 0.02	95.4/98
MOS1+2	$6.4^{+0.7}_{-0.6}$	$0.34^{+0.14}_{-0.13}$	0.975^1	96.8/99

[1] Fixed redshift.

therefore we assume that XMM1229 is a cluster with a standard X-ray morphology i.e., without signs of merging or a strong cool core and use the typical values $\beta = 0.7$ and $r_c = 250$ kpc, obtaining L_X ($r < 2$ Mpc) $\sim 3 \times 10^{44}$ erg s^{-1}.

2.2. HST/ACS i_{775} and z_{850} band imaging

In the framework of the Supernova Cosmology Project (Dawson et al. 2009), we obtained HST/ACS Wide Field Camera (WFC) data. Images in the *F775W* (i_{775}) and *F850LP* (z_{850}) passbands centred on the cluster X-ray centroid were acquired in December 2006, with total exposures of 4110 s and 10 940 s, respectively. The i_{775} and z_{850} are the most efficient filters in supernova searches and, although they are not optimal for a cluster at this redshift, the i_{775} encloses the D4000 break, which is redshifted to 7920 Å at the cluster redshift. ACS has a field of view (FoV) of 3.3×3.3 arcmin and a pixel scale of 0.05″/pix. The images were processed using the ACS GTO *Apsis* pipeline (Blakeslee et al. 2003b), with a *Lanczos*3 interpolation kernel. The photometric zero points are equal to 34.65 and 34.93 in the i_{775} and z_{850} bands, respectively, following the prescription of Sirianni et al. (2005). To account for Galactic extinction, we applied to our photometric catalog the correction factor $E(B-V) = 0.017$ retrieved from the NASA Extragalactic Database[2] for the dust extinction maps of Schlegel et al. (1998). The corresponding correction in the optical bands is $E(i_{775} - z_{850}) = 0.010$ mag.

2.3. VLT/FORS2 spectroscopy

Spectroscopic observations were carried out with the Focal Reducer and Low Dispersion Spectrograph (FORS2: Appenzeller et al. 1998) on Antu (Unit 1 of the ESO Very Large Telescope (VLT)) as part of a program to search for very high-redshift type Ia supernova in the hosts of early-type galaxies of rich galaxy clusters (Dawson et al. 2009). In this respect, the field XMMU J1229+0151 was very rich in candidates, with three candidates occurring during the three months of monitoring. One candidate was identified as a type Ia supernova at the cluster redshift (Dawson et al. 2009).

FORS2 was used with the 300I grism and the OG590 order-sorting filter. This configuration has a dispersion of 2.3 Angstroms per pixel and provides a wavelength range starting at 5900 Å and extending to approximately 10 000 Å. Since the observations had to be carried out at short notice (the SN had to be observed while it was near maximum light), most of the observations were completed with the multi-object spectroscopic (MOS) mode of FORS2. The MOS mode consists of 19 moveable slits (with lengths that vary between 20″ and 22″) that can be inserted into the focal plane. The slit width was set to 1″. On one occasion, when the MOS mode was

Table 3. FORS2 observing Log.

Mask	Type	Slits	Grism & Filter	T_{exp} (s)	Airmass	Date (UT)
1	MOS	12	300I+OG590	8×750	1.3	2006 Jan. 01
2	MOS	18	300I+OG590	8×700	1.2	2006 Jan. 30
3	MOS	18	300I+OG590	4×700	1.1	2006 Jan. 31
4	MOS	18	300I+OG590	4×700	1.2	2006 Feb. 01
5	MXU	34	300I+OG590	9×900	1.3	2006 Jun. 20−21

unavailable because of technical reasons, the field was observed with the MXU mode of FORS2. The MXU mode involves the insertion of a precut mask into the FORS2 focal plane once the field has been acquired. Since the length of the slit can be far shorter in the MXU mode than in the MOS mode, the number of targets that could be observed in the MXU mode was a factor of two higher than the number of targets that could be observed in the MOS mode. However, the time to prepare, cut, and insert a mask is usually a couple of days, whereas the MOS observations can be done with a few hours notice.

The field of XMMU J1229+0151 was observed with five different configurations, 4 MOS and one MXU. The details of the observations are given in Table 3. The MOS configurations were used when the supernovae (there were three supernova visible in the field of XMMU J1229+0151 at the same time) were near maximum light. The MXU mask was used several months later when the supernovae were significantly fainter. In all masks, slits were placed on the supernova, and hence both spectra of the supernovae and their hosts and spectra of the hosts without the supernovae were obtained. The other slits were placed on candidate cluster galaxies or field galaxies. For each MOS setup, between 4 and 9 exposures of 700 to 900 s were taken. Between each exposure, the telescope was moved a few arcseconds along the slit direction. These offsets, which shift the spectra along detector columns, allow one to remove detector fringes, as described in Hilton et al. (2007), which also describes how the FORS2 data was processed.

A total of 100 slits over four masks were used to observe 74 individual targets. The targets were selected by colour and magnitude, using the R- and z-band pre-imaging. Priority 1 targets had $(R-z) > 1.8$ and $z < 23$, and priority 2 targets had $1.8 < (R-z) < 1.6$ and $z < 23$. Some cluster members were observed in more than one mask. For these 74 targets, 64 redshifts were obtained, and 27 of these are of cluster members – the redshift distribution of the targets in shown in Fig. 3. A total of 21 confirmed member galaxies are within the FoV of ACS.

Cluster membership was attributed by a reasonable selection of galaxies within ± 2000 km s^{-1} relative to the peak of the redshift distribution, or ~ 3-σ. We assigned the mean value of the redshift distribution of the 27 cluster members to the cluster redshift, $z = 0.975$ and assumed a conservative redshift error of $\Delta z = 10^{-3}$. The cluster velocity dispersion was determined with the 27 galaxy redshifts, using the software ROSTAT of Beers et al. (1990). We obtained $\sigma = 683 \pm 62$ km s^{-1}, where the error refers to the formal boostrap error obtained with 1000 samples. This value is in perfect agreement with the result obtained using the methodology proposed by Danese et al. (1980).

Even though we have a limited number of cluster members which could introduce a bias in our computation of σ due to the presence of substructures, we, nevertheless, investigate the connection between the state of the hot intra-cluster medium (ICM) and the cluster galaxy population by means of the well-known temperature−σ relation (e.g., Wu et al. 1999). The observed
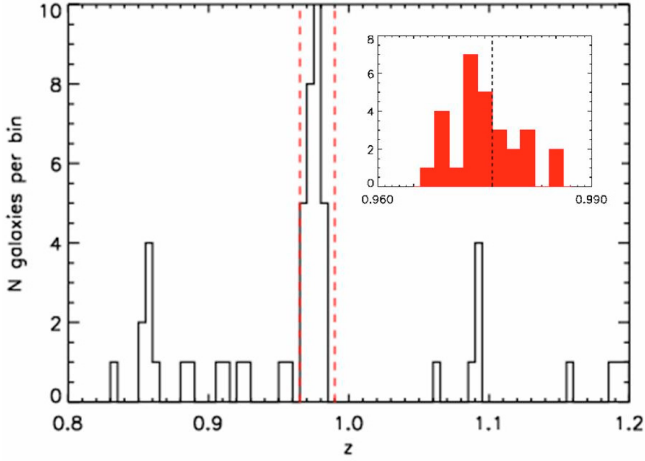
Fig. 3. Redshift distribution of the galaxies in the cluster XMMU J1229+0151. Vertical red-dashed lines refer to redshift cuts at $z = 0.965, 0.990$ used to select the cluster members. This region is shown in more detail in the top-right inset.

$T-\sigma$ relation for high-z clusters (e.g., Rosati et al. 2002) implies that we would expect a higher velocity dispersion of about 900 ± 300 km s^{-1} for the cluster temperature. We note however that there is significant scatter in the $T-\sigma$ relation, and that our value is within the 30% scatter.

In Table 4, we list the cluster members. The information provided is the following: galaxy ID (Col. 1); RA (Col. 2) and Dec (Col. 3); redshift (Col. 4); spectral classification (Col. 5) and morphological type (Col. 6). The spectral classification is done according to the scheme proposed in Dressler et al. (1999), based on the strength of the [OII] and H$_\delta$ lines. The k class refers to passive (no [OII] emission) galaxies. This class is subdivided into two types, depending on the strength of the H$_\delta$ lines: k+a have moderate ($3 < EW$ H$_\delta < 8$) H$_\delta$ absorption, and a+k show strong (EW H$_\delta > 8$) H$_\delta$ absorption. The e spectral class refers to galaxies with [OII] emission and is subdivided into three types: e(a) exhibit strong Balmer absorption; e(c) have weak or moderate Balmer absorption; and e(b) show very strong [OII] lines.

2.4. NTT/SOFI J- and Ks-band imaging

NIR imaging in the J- and Ks-bands were acquired using SOFI (Moorwood et al. 1998) at the New Technology Telescope (NTT) at the ESO/La Silla observatory. The observations were taken in March 2007, as part of the NIR follow-up of the XDCP survey programme. The instrument was operated in the *Large field* mode, corresponding to a 5×5 arcmin FoV, with a pixel scale of 0.288 arsec/pix. Since the NIR background is generally highly variable, a large dithering pattern has to be applied, thus we set the automatic jitter box to have a width of 30 arcsec. Total exposure times were 1hr in Ks and 45 min in J. The J-band data have a seeing of 0.98″, whereas the Ks-band have an image quality of 0.69″.

Photometric calibration standards (Persson et al. 1998) were acquired several times during the observation run. The zero points (ZP) were computed using the reduced standards (background subtracted, count rate image) with the following relation:

$$ZP = mag + 2.5 \log(count\ rate) + atm_{corr} * airmass \qquad (1)$$

where mag refers to the standard star magnitude, and atm$_{corr}$ refers to the wavelength dependent atmospheric correction. The stellar flux was measured within circular apertures of 6″ radius;

Table 4. Spectroscopic confirmed members.

ID	RA (J2000)	Dec (J2000)	z	Class	Type
(1)	(2)	(3)	(4)	(5)	(6)
5417	187.3857875	1.8712528	0.977	a+k	S0
3428	187.3793000	1.8563222	0.984	a+k	S0
3430	187.3720375	1.8560639	0.974	k	Ell
3025	187.3771333	1.8363889	0.979	e(c)	Ell
4055	187.3573750	1.8601056	0.968	k	Sb
3301	187.3466250	1.8502667	0.969	e(c)	Ell
4155	187.3885500	1.8644889	0.969	k+a	Ell
5411	187.3718958	1.8717778	0.974	k	Ell
20008	187.3734583	1.8726667	0.973	e(a)	Irr
3497	187.3724875	1.8579083	0.982	a+k	Ell
20010	187.3726625	1.8579944	0.977	k	Ell
4126	187.3900292	1.8628750	0.973	k	Ell
3507	187.3716250	1.8571444	0.976	k	Ell
20013	187.3684167	1.8559167	0.979	k	Ell
20014	187.3654583	1.8485556	0.969	k	S0
3949	187.3696083	1.8602611	0.976	k	Ell
30004	187.3697875	1.8601389	0.970	k	S0/Ell
3495	187.3715708	1.8582111	0.980	k	Ell
3524	187.3807000	1.8676667	0.969	a+k	Ell
5499	187.3844542	1.8683722	0.973	k	Ell
3205	187.3747292	1.8461806	0.984	a+k	Ell
4661[a]	187.3631292	1.8977194	0.975	k+a	–
5001[a]	187.3500083	1.8870944	0.973	k	–
4956[a]	187.3367208	1.8890611	0.978	k	–
4794[a]	187.3342500	1.8927333	0.974	k	–
4910[a]	187.3213042	1.8925528	0.976	e(b)	–
4800[a]	187.3186708	1.8948944	0.976	k	–

[a] Galaxy outside the FoV of ACS.

this large radius ensured that the bulk of the galaxy flux in included. The background was estimated with a 3σ clipping algorithm. The scatter in the zero points is 0.015 mag and 0.04 mag for the J and Ks filter, respectively. We converted VEGA magnitudes to the AB photometric system with an ESO web-tool[3].

The data was reduced with the package ESO/MVM (Vandame 2004) using the HST/ACS catalog to match the astrometry. We used SExtractor (Bertin & Arnouts 1996) in *dual-image mode* to perform the source detection in the Ks-band, and the photometry of both images.

3. Structural analysis

In this section we determine the structural parameters and morphological class of the cluster galaxies.

3.1. Surface-brightness profile fitting

The radial surface-brightness profiles of galaxies can be described by the Sersic law (Sersic 1968),

$$\Sigma(r) \propto \exp(r/r_e)^{1/n} - 1 \qquad (2)$$

where $\Sigma(r)$ is the surface brightness at radius r, the Sersic index, n, characterizes the degree of concentration of the profile; and the effective radius, R_e, corresponds to the projected radius enclosing half of the galaxy light.

Using the ACS i_{775} and z_{850} data we completed a 2D bulge/disk galaxy decomposition with the software GIM2D (Simard et al. 2002). The galaxy model is the sum of a bulge component (Sersic profile) and an exponential disk, depending

[3] http://archive.eso.org/apps/mag2flux
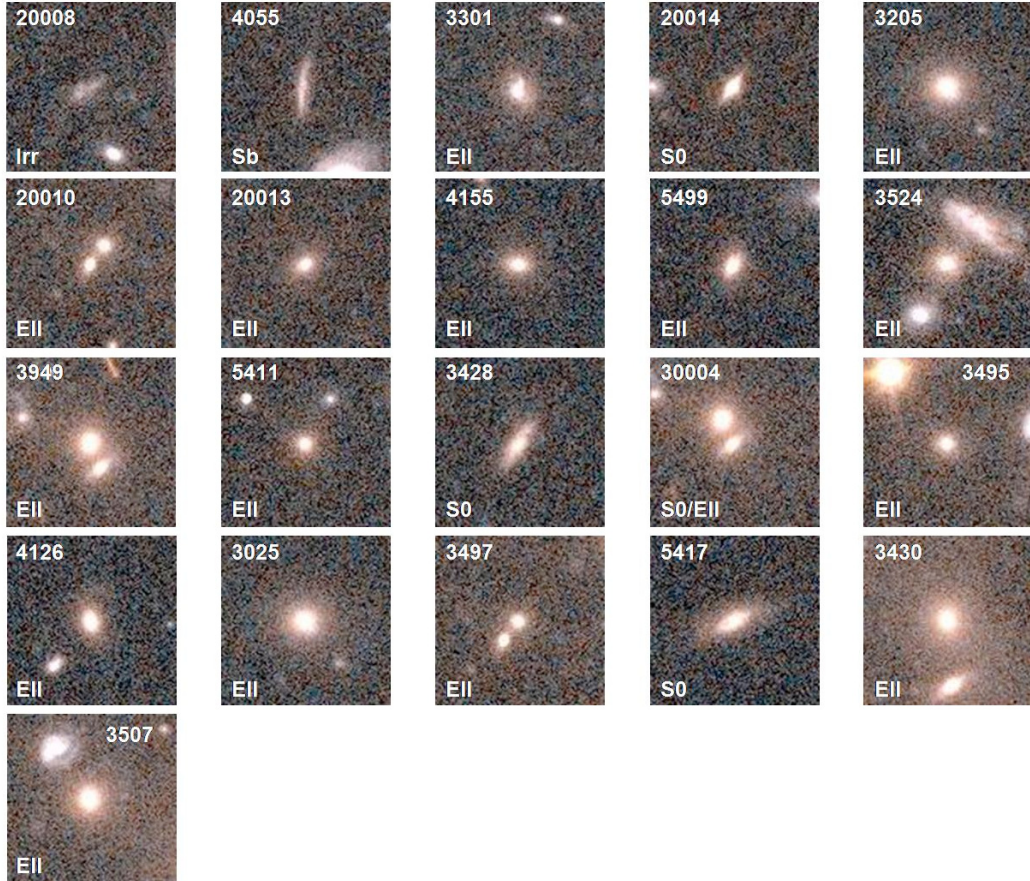
Fig. 4. $i_{775} - z_{850}$ image gallery of the 21 spectroscopically confirmed members in the ACS FoV, ordered in increasing $i_{775} - z_{850}$ colour. Individual stamps are centred on the cluster members and have a size of $5'' \times 5''$. Top labels correspond to the spectroscopic galaxy ID and bottom labels refer to the visual morphological classification.

on a total of eleven parameters. Of these parameters, three describe the shape of the Sersic profile, including the index n, which we constrained to be $0 < n < 4$. The upper bound was introduced because $n = 4$ corresponds to the de Vaucouleurs profile, a purely empirical fit to the profiles of elliptical galaxies and bulges (de Vaucouleurs 1961). Allowing higher values of n usually does not improve the fit, although the covariance between n and R_e can lead to an overestimation of R_e for high n (Blakeslee et al. 2006). The median Sersic index n of the spectroscopically confirmed galaxies is 3.9 and the median effective radius is 5.5 pixel ($0.28''$).

The distribution of R_e is consistent in both bands within the 1-σ errors, and has an average error of 0.77 and 0.53 pix in the i_{775} and z_{850} band, respectively. The comparison between the effective radii obtained in the two bands R_e (i_{775})$-R_e$ (z_{850}) is shown in Fig. 5. This difference is useful in assessing an imperfect match of the PSFs or the presence of colour gradients. However, we find a very good agreement between the two radii and therefore do not expect to observe these effects. In this figure, we also present the results of fitting a "red-sequence" sample of early-type galaxies that is introduced in Sect. 4.2. The reduced χ^2 of the best-fit models is ~1 for the majority of the galaxies, emphasizing the good quality of the fit.

3.2. Visual morphological classification

In addition to the profile fitting, we completed a visual classification of the spectroscopic members using morphological templates from Postman et al. (2005). In Fig. 4, we show postage stamps of the cluster members in the i_{775} passband labelled with the morphological type. We note two red galaxy pairs (ID = 20010/3497, 30004/3949). In Fig. 6, we show the distribution of the fit parameters n and R_e of both the spectroscopic and "red-sequence" samples (see Sect. 4.2 for details of the latter), complemented with the visual classification.

The morphology of the spectroscopic galaxies in XMM1229 is clearly dominated by elliptical galaxies (15/21) with only one galaxy classified as spiral (ID = 4055) and one irregular (ID = 20008), unlike other distant clusters (see for e.g., the EDisCS high-redshift sample, $z \leq 0.8$, De Lucia et al. 2004). The remaining four cluster members are classified as S0s. We stress that we targeted red galaxies for spectroscopy and hence applied a colour, and not a morphological selection. We, therefore, do not expect to be biased more towards ellipticals than later-type galaxies such as S0s.

4. The $i_{775} - z_{850}$ colour–magnitude relation

4.1. Galaxy photometry

We used SExtractor in *dual-image mode* to perform the source detection in the z_{850} band, and the photometry in both bands. The image quality of the i_{775} band is sightly superior to that of the z_{850} band, with a Point Spread Function (PSF) FWHM of $0.085''$, as opposed to $0.095''$ in the z_{850}. The effect of the z_{850} PSF broadening has been investigated in other works
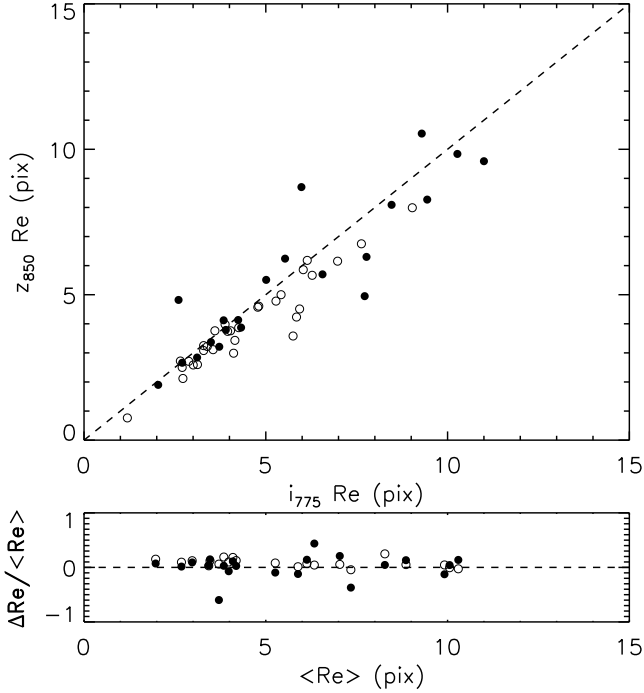
Fig. 5. Comparison of the R_e obtained with GIM2D in the i_{775} and z_{850} bands. Spectroscopic members are represented in solid circles and "red-sequence" galaxies (see Sect. 4.2) are shown in open circles. The dashed line indicates the one-to-one relation. The bottom plot shows the difference in the R_e values for the two bands normalized by the average R_e. The dashed line represents the constant zero value.
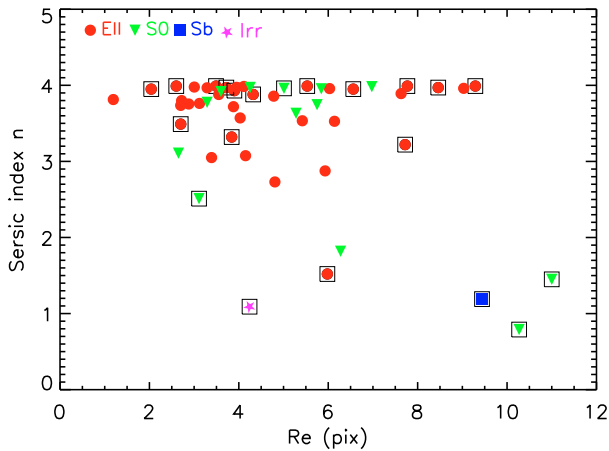
Fig. 6. Sersic index n as a function of the effective radius R_e obtained with GIM2D, using the ACS/i_{775} band. The spectroscopic sample is indicated by open squares. The morphology of the cluster members is dominated by elliptical galaxies (red circles) characterized by a high n. Four galaxies are classified as S0 (green triangles), one member is an Sb galaxy (blue square), with $n < 1$ and one galaxy has an irregular shape (magenta 5-pointed star). The 31 "red-sequence" early-type galaxies (see Sect. 4.2) are also displayed with the same symbols without the open squares.

(e.g., Mei et al. 2006) and is attributed to the long-wavelength halo of the ACS/WFC (Sirianni et al. 2005). This effect, although small, has implications for the galaxy colour measurement and must be accounted for. Thus, for each passband we constructed empirical PSFs by computing the median profile of a handful of stars in the science images for which we measure growth curves normalized to the central intensity. We obtained a differential
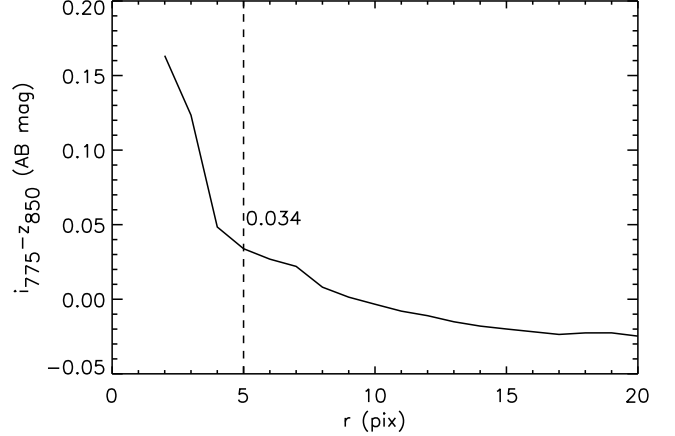
Fig. 7. Differential PSF blurring effect in i and z-bands: at $r = 5$ pix (0.25 arcsecs) the PSF correction is 0.034 mag (vertical line).

($z_{850} - i_{775}$) median radial profile that shows a steep behaviour for radii smaller than 3 pix (see Fig. 7).

The $i_{775} - z_{850}$ colour was determined in small apertures to avoid the effects of intrinsic galaxy colour gradients (see e.g., Scodeggio 2001, for a discussion on the effect of internal colour gradients). We chose a fixed aperture of 5 pix (0.25″) since at this radius the steep and uncertain PSF broadening is no longer dominant (see Fig. 7), and we apply a correction of 0.034 mag to the i_{775} band to match the poorer seeing of the z_{850} band. Total z_{850} band magnitudes were obtained from the SExtractor parameter MAGAUTO.
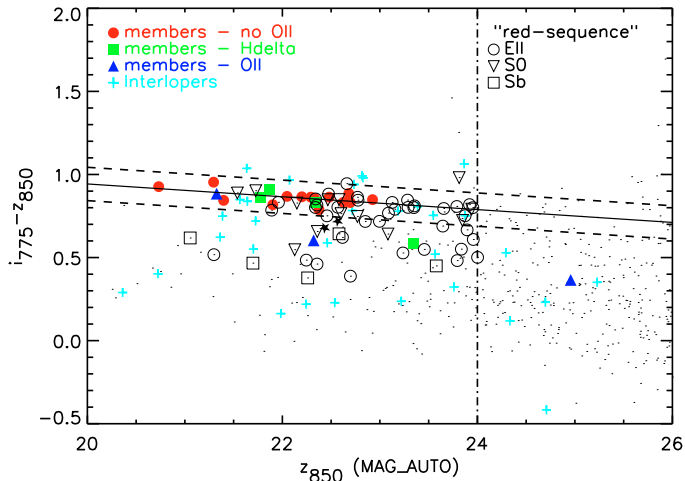
4.2. Colour–magnitude relation

The colour–magnitude relation is presented in Fig. 8. We flag the 35 confirmed interlopers in the ACS field (cyan crosses), since nearly a fourth of them (9/35) are located on the red-sequence.

We performed a robust linear fit using bi-square weights (Tuckey's biweight) to the CMR of the confirmed passive members. The bi-square weights were calculated using the limit of 6 outlier-resistant standard deviations. The process was performed iteratively until the standard deviation changes by less than the uncertainty in the standard deviation of a normal distribution. The linear fit has a slope of -0.039 ± 0.013 and a zero point of 0.86 ± 0.04, which was determined to be the bi-weight mean. The quoted uncertainty in the slope corresponds to the estimated standard deviation of the fit coefficient. The scatter in the CMR including only the passive galaxies is 0.039 mag.

Since the spectroscopic sample does not populate well the faint end of the red-sequence, we selected a "red-sequence" sample, based on a combination of morphological and colour criteria. We applied a generous colour cut of $0.5 < i_{775} - z_{850} < 1.3$ for $20 < z_{850} < 24$, based on the properties of the bluest star forming cluster galaxies and the magnitude limit set by Postman et al. (2005) to ensure a reliable morphological classification. In addition, we constrained the search radius to be 1′ from the cluster X-ray center, corresponding to 478 kpc at the cluster redshift. This is a reasonable area to search for cluster members, and avoids contamination by non-members. We can also express this radius as a fraction of the fiducial radius R_{200} estimated using the $R_{200} - T$ X-ray scaling relations of Arnaud et al. (2005). Thus, we determine the search radius of 478 kpc to be equal to $0.4 \times R_{200}$.

We found 58 galaxies in this region which were visually classified using the templates from Postman et al. (2005).
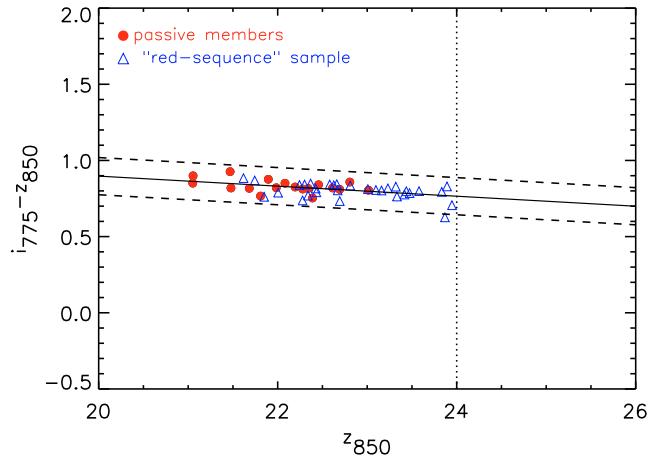
Fig. 8. $i_{775} - z_{850}$ colour–magnitude relation of XMM1229. The black solid line refers to the linear fit to the passive cluster members, which are shown in red circles. The dashed lines correspond to the 3-σ region. The confirmed galaxies with [OII] emission are displayed in blue triangles; members with strong Hδ absorption (see Sect. 5.2) are displayed in green squares. The cyan crosses refer to spectroscopically confirmed interlopers. The "red-sequence" sample is presented with open black symbols: circles refer to ellipticals, squares refer to S0s, and inverted triangles correspond to Sb galaxies. A merging pair of elliptical galaxies is marked with two filled 5-pointed-stars. The black dots correspond to objects within 1 arcmin of the X-ray cluster center.

The selection of the red-sequence galaxies was based on a 3-σ clipping about the linear fit to the colour–magnitude relation of the confirmed passive members. Thirty-one galaxies are in the region delimited by the 3-σ clipping, for a z_{850} magnitude cut at 24 mag. Again the fraction of ellipticals, 22/31, is much higher than the fraction of S0s, 9/31. The scatter in the red-sequence combining the two samples (spectroscopic and "red-sequence") is equal to 0.048 mag.

4.3. Model colour–magnitude relation

Traditionally, galaxy colours are measured by using either aperture magnitudes with corrections which take into account PSF differences, or aperture magnitudes after deconvolving the PSF as, for e.g., in Blakeslee et al. (2003a). We instead explored a method for deriving galaxy colours based on model magnitudes, as commonly used in the *Sloan Digital Sky Survey* (e.g., Blanton et al. 2005). In this method, the PSFs of the 2 filters (which are estimated independently in the two bands as described in the previous section) are convolved with the galaxy profile models. Hence, this is a direct method where convolution and *not* deconvolution is performed. We therefore used the surface brightness best-fit models with additional Gaussian noise to measure aperture and total magnitudes. In a similar way to the "data" CMR (Sect. 4.2), the colour measurements were derived for fixed apertures of $r = 5$ pix. An alternative approach would be to measure aperture magnitudes over the individual galaxy effective radius, although this strategy has proven unreliable because for many galaxies R_e is smaller than 3 pix (0.15''), which is really too small to make a proper colour measurement. Total magnitudes were derived using apertures with a radius of $10 \times R_e$ instead of using SExtractor MAG_AUTO, which we found to be inaccurate compared to large aperture magnitudes. These

Fig. 9. $i_{775} - z_{850}$ colour–magnitude relation of XMM1229 using the best-fit galaxy models. The black solid line refers to the composite linear fit to both the passive cluster members (red circles). The dashed lines delimit the 3-σ region and the dotted line marks the z_{850} magnitude cut at 24 mag.

discrepancies are visible in the total z_{850} magnitude of the brightest galaxies in the two CMR's represented in Figs. 8 and 9.

The procedure used to fit the CMR and obtain its zero point was identical to the method described earlier in Sect. 4.2, except that now we use both the early-type cluster members and the "red-sequence" sample. If we consider only the confirmed passive members in performing the linear fit, we obtain a zero point $CMR_{ZP} = 0.83 \pm 0.04$, a slope of -0.031 ± 0.016, and a scatter equal to 0.042 ± 0.011. The error in the scatter was estimated with 100 Monte Carlo simulations of the galaxy models, varying the Sersic index and the effective radius within the 1-σ confidence errors. The uncertainty associated with the scatter was estimated by fitting a Gaussian to the distribution of the scatter measured in the models and assigning the standard deviation of the distribution to be the error. To perform a composite linear fit to both the spectroscopic and "red-sequence" samples, we applied a magnitude cut at $z_{850} = 24$ mag, a limit that ensures a reliable visual classification of the "red-sequence" sample (see for e.g., Postman et al. 2005). We obtain a CMR zero point equal to 0.81 ± 0.04, the total intrinsic scatter slightly increases to 0.050 mag and the slope, -0.031 ± 0.008, remains nearly unchanged.

We note that the scatter in the colour–magnitude relations derived from SAM is a factor 2−3 higher than the observational scatter (see for e.g., Menci et al. 2008). In semi-analytical modelling the scatter is measured by computing the total galaxy magnitudes, which is known precisely in simulations. A possible reason for the discrepancy between the observational scatter and that obtained with simulations is the existence of colour gradients, which are taken into account in the total galaxy magnitudes used in SAM to measure the scatter, whereas in the observations we limit the colour measurement to a small central aperture, which minimizes the effect of such gradients. To investigate this effect, we measured the $i_{775} - z_{850}$ colour of the passive members using the galaxy models, by increasing the fixed colour aperture to $r = 10, 15$ pix, i.e., 0.5'', and 0.75'' respectively. Going beyond these radii would produce noisy measurements since we would run into the background. The corresponding scatter is then 0.068, and 0.088, respectively, which suggests the presence of colour gradients in the galaxy sample.

5. Analysis of the spectral energy distributions

The observed spectral energy distribution of a galaxy is a record of its stellar population history. The SED fitting method relies on the comparison of the observed SED with synthetic SED's. The latter are then convolved with the transmission curves of the filters used in the observations and the output magnitudes are compared with the observed magnitudes. Galaxy SED's were determined by measuring the flux within a fixed aperture of 3 arcsec in the four available passbands.

Given the large disparity in the resolution of the ground- and space-based data, a careful matching of the different PSFs must be done when constructing the multi-wavelength catalog for sampling the galaxies' SEDs. The method we used to derive aperture corrections is the following: we smoothed the i_{775}, z_{850}, and Ks-band images with Gaussian kernels to match the seeing of the J-band ($\sim 1''$) and made growth curves of stars in the original and degraded (smoothed) images. We then obtained a differential median radial profile for each band with which we derived corrections at a given radius. In the multi-colour catalog, we used galaxy magnitudes corrected to match the fluxes to the worst seeing image (J-band), measured within $0.5''$ radius apertures for the ACS bands, and $1.16''$ for the NIR data. We opted to work with magnitudes extrapolated to a $3''$ radius, which safely enclose the bulk of the galaxy flux.

A total of 20 spectroscopic members are common to the FoV of SOFI and ACS, four of which constitute two red galaxy pairs that are not properly resolved in the NIR data. For this reason, we had to exclude them from the spectral analysis. Only four of the remaining 16 studied galaxies show [OII] emission lines (IDs: 3025, 3205, 3301, 4055) signaling ongoing star-formation, and the first two also present [OIII] lines. The first three galaxies were visually classified as ellipticals, although galaxy 3301 has a low Sersic index, $n = 1.5$. Galaxy ID = 4055 is an edge-on spiral, which is reflected in its low Sersic index ($n = 1.2$).

We also fitted the SEDs of the ETGs in the "red-sequence" sample lying on the ACS CMR red-sequence. As mentioned earlier, we find 31 ETG in the locus of the red-sequence. The poorer quality of the NIR data can only resolve 18 of these galaxies.

### 5.1. Spectrophotometric properties: masses, ages

Stellar masses, ages, and star-formation histories are derived from the synthetic galaxy fluxes, assuming solar metallicity and a Salpeter (Salpeter 1955) initial mass function (IMF), with a mass cut off [0.1–100] $M_\odot$. We perform a three parameter (age T, τ, mass) fit to the SEDs using a grid of Bruzual & Charlot (2003) models characterized by a delayed exponential star-formation rate: $\frac{t}{\tau^2} \cdot \exp(\frac{-t}{\tau})$, performing a minimization of the χ^2. The parameter τ spans a range of [0.2–5.8] Gyr, where 5.8 Gyr is the age of Universe at the cluster redshift. As an example, in Fig. 10 we present the fit to the SED of 3025, one of the three brightest galaxies (see Sect. 6), together with the filter transmission curves.

The star-formation (SF) weighted age represents the mean age of the bulk of the stars in a galaxy (depending on the τ parameter), and is defined as

$$t_{\rm SFR} = \frac{\int_0^T {\rm d}t' (T - t') \Psi(t')}{\int_0^T {\rm d}t' \Psi(t')}, \tag{3}$$

where Ψ is the star-formation rate expressed as

$$\Psi = \tau^{-2} t {\rm e}^{\frac{-t}{\tau}} + A\delta(t - t_{\rm burst}). \tag{4}$$
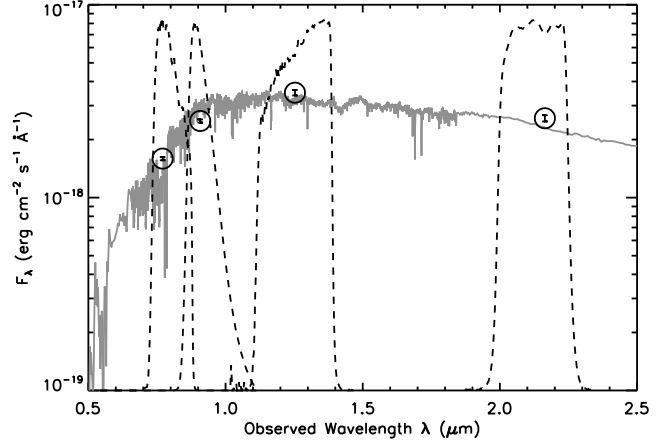
Fig. 10. SED fit of one of the three brightest galaxies, ID = 3025 (solid line). The flux measurements in the i_{775}, z_{850}, J, and Ks-bands (respectively from left-to-right) are shown in circles, with 1-σ error bars, along with the filters transmission curves (dashed lines).

Table 5. SED analysis of the spectroscopic members.

Galaxy ID (1)	Mass (10^{10} $M_\odot$) (2)	$t_{\rm SFR}$ Age (Gyr) (3)
3301	$5.3^{+1.8}_{-3.1}$	$4.09^{+0.34}_{-2.82}$
4055	$1.8^{+1.1}_{-1.3}$	$3.94^{+0.58}_{-3.14}$
20014	$2.4^{+2.2}_{-0.3}$	$1.18^{+1.34}_{-0.1}$
20013	$4.9^{+0.8}_{-2.0}$	$4.18^{+0.18}_{-2.19}$
5411	$6.4^{+2.3}_{-2.7}$	$4.55^{+1.19}_{-2.15}$
3507	26^{+2}_{-11}	$5.74^{+0}_{-2.50}$
3495	$7.4^{+3.6}_{-2.8}$	$4.46^{+1.28}_{-2.06}$
3430	23^{+3}_{-11}	$5.74^{+0}_{-2.84}$
3205	$8.3^{+0.3}_{-2.3}$	$3.86^{+0.15}_{-1.56}$
3524	18^{+2}_{-11}	$5.99^{+0}_{-3.80}$
3428	$6.5^{+1.0}_{-2.7}$	$4.27^{+0.19}_{-2.17}$
3025	20^{+6}_{-9}	$4.85^{+0.89}_{-2.36}$
5417	$8.9^{+5.1}_{-1.8}$	$3.49^{+2.25}_{-0.64}$
5499	$8.3^{+3.7}_{-3.7}$	$4.27^{+0.68}_{-2.28}$
4155	$6.8^{+0.9}_{-2.7}$	$4.43^{+0.18}_{-2.24}$
4126	$6.8^{+1.3}_{-0.8}$	$2.50^{+0.91}_{-0.31}$

The parameter A refers to the amplitude of an instantaneous burst at time $t_{\rm burst} > \tau$, as described in Gobat et al. (2008). Galaxy SF-weighted ages do not change significantly if other models (Maraston 2005) and different IMF's are used (Chabrier 2003; Kroupa & Weidner 2003), although the stellar masses are dependent on the chosen IMF.

The spectroscopic cluster members form a fairly old population, with a median SF weighted age of 4.3 Gyr, and stellar masses in the range 4×10^{10}–2.3×10^{11} $M_\odot$ (see Table 5 for the listing of the fitted masses (Col. 2) and ages (Col. 3)). The "red-sequence" sample, which allows us to probe fainter galaxies, appears to be less massive, with a median stellar mass of 5.5×10^{10} $M_\odot$. However, since we do not have redshifts for these galaxies, we cannot draw strong conclusions about their masses and formation ages.

In Fig. 11, we investigate the correlation between the star-formation-weighted age and stellar-mass content in both the spectroscopic (filled circles) and "red-sequence" samples (open circles). We identified a strong mass-age correlation, which was confirmed with a Spearman *rho* rank of 0.61 with a
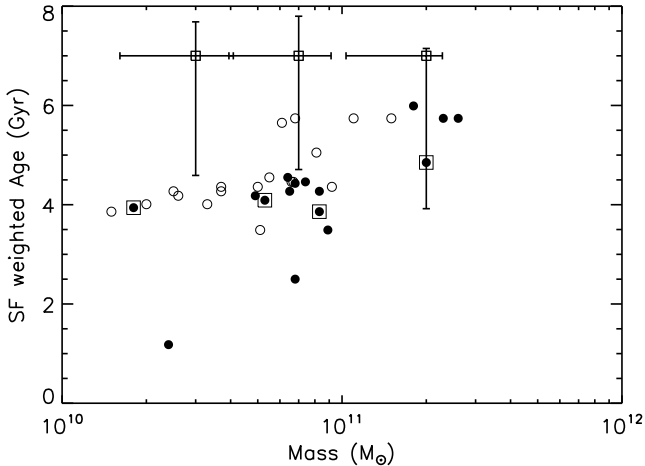
Fig. 11. Photometric masses of the 16 spectroscopic cluster galaxies (filled circles) and 18 "red-sequence" ETGs (open circles) as a function of their star-formation-weighted ages. Spectroscopic members with [OII] emission or morphologically classified as late-type galaxies are indicated by square symbols. Mean error bars corresponding to three mass bins (bin1: $m < 4.5 \times 10^{10}\ M_\odot$, bin2: $4.5 \times 10^{10}\ M_\odot < m < 1 \times 10^{11}\ M_\odot$, bin3: $m > 1 \times 10^{11}\ M_\odot$) are shown at the top of the figure.

significance p of 1.4×10^{-4} (p is a value lying in the range [0.0−1.0], where $p = 0$ indicates a very significant correlation and $p = 1$ means no correlation). This mass-age correspondence is consistent with a well-known anti-hierarchical behaviour (*downsizing*), where the most massive galaxies are also the oldest.

We also investigated the dependence of mass and SF weighted age with the galaxy radial distance from the cluster center. We found that the most massive elliptical galaxies reside at the cluster core, and conversely the four late-type galaxies are situated at the periphery of the cluster, at about 1 arcmin from the center, indicating that star-formation is taking place in these regions. This morphological segregation is well established at lower redshifts (e.g., Biviano et al. 2002), although it is interesting to note that at redshift ~1, the late-type galaxies are already settled at the outskirts of the cluster. This segregation was also found by Demarco et al. (2005) and Homeier et al. (2005) in the study of a cluster with $z = 0.837$, as well as in RDCS 1252.9-2927 at $z = 1.234$ (Demarco et al. 2007). The dependence of the star-formation-weighted age with the clustercentric distance (Fig. 12) shows that the galaxy age scatter increases at larger radii. This is indicative of younger/more diverse SF histories for galaxies located in the outer regions of the cluster, which have presumably been accreted later onto the cluster. This result has also been found in other work, e.g., Mei et al. (2009).

Finally, we analysed the relation between the $i_{775} - z_{850}$ colour and the galaxy stellar mass (Fig. 13) and we observed the expected trend of the most massive galaxies being redder.

5.2. Star formation histories

The spectra of 12 confirmed passive members were coadded to obtain the stacked spectrum. However, four (ID = 3428, 3524, 4155 and 5417) of these 12 galaxies have strong H_δ absorption, $EW(H_\delta) \geq 3$ (these are a+k/k+a spectral types, see Table 4) and we therefore removed them from the stacking procedure. Three of these galaxies are at about 1 arcmin from the X-ray cluster center and only galaxy (ID = 3428) is closer to the core, at
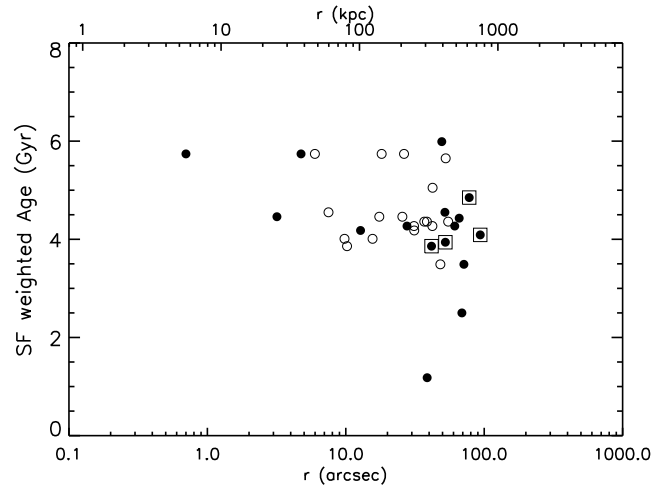

Fig. 12. SF weighted age *versus* radial distance to the cluster center. Spectroscopic members with [OII] emission or morphologically classified as late-type galaxies are indicated by square symbols.
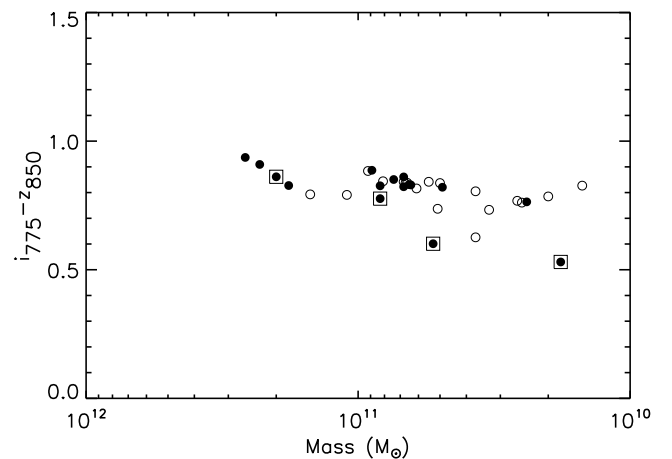
Fig. 13. Correlation between galaxy $i_{775} - z_{850}$ colour and photometric mass. Spectroscopic members with [OII] emission or morphologically classified as late-type galaxies are indicated by square symbols.

~0.5 arcmin from the center. In Fig. 14, we present the coadded spectrum of 8 spectroscopic passive members with weak or no H_δ absorption. The best-fit SED is shown in green and the spectral fit is shown in red.

Star-formation histories were derived only for the eight galaxies that do not have significant H_δ absorption. The star-formation-weighted age and formation redshift obtained by the best-fitting models (i.e., those within the 3-σ confidence), is $3.7^{+0.4}_{-0.5}$ Gyr and $z_f = 3.0 \pm 0.5$ respectively, when using the combined spectrophotometric data. It is not surprising that there is discrepancy between the average age obtained by fitting the individual SEDs (4.3 Gyr) and that derived from the composite spectrophotometric data, since we used the spectrum and SED to place complementary constraints on the star-formation histories (the former has resolution but poor wavelength coverage, while the latter has coverage but poor resolution). This discrepancy can stem from the fact that the SED unfortunately does not probe the rest-frame UV and would thus be somewhat insensitive to recent star-formation.
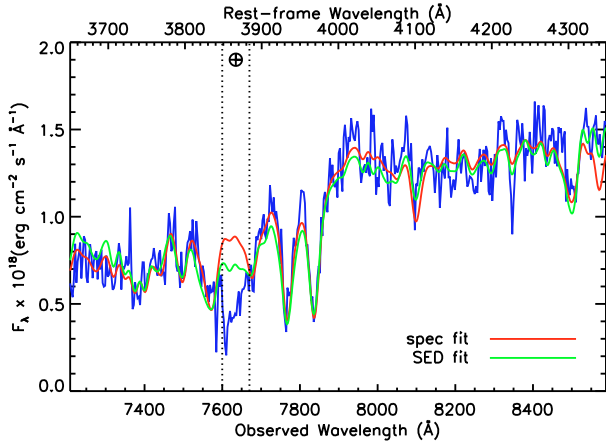
Fig. 14. Stacked spectrum (in blue) of all passive members which do not show strong H_δ absorption (k type, see Table 4). The red line refers to the best-fit model to the stacked spectrum and the green line refers to the best-fit model to the average SED. The region around the atmospheric A-band at 7600 Å (dashed lines) is difficult to subtract and was therefore ignored in the fit.

6. Is there a brightest cluster galaxy?

The cores of rich galaxy clusters often host a massive, bright, giant elliptical galaxy which is called the brightest cluster galaxy (BCG). In XMM1229, we found three bright galaxies within ~0.5 mag, instead of one prominent BCG. The total z_{850}-band magnitudes were derived by integrating the best-fit surface brightness model to a large galaxy radius, $r = 10 \times R_e$. In Table 6, we summarize the most relevant characteristics of these galaxies: total z_{850} magnitude from best-fit model (Col. 2), distance to the X-ray cluster center (Col. 3), photometric mass (Col. 4), star-formation weighted age (Col. 5). As expected, the three bright galaxies are the most massive galaxies, with masses of the order of 2×10^{11} $M_\odot$. The galaxy ID = 3025 located at $1.3''$ from the cluster center shows strong [OII] emission, indicating ongoing star formation confirmed by a lower star-formation-weighted age of 4.85 Gyr, which is approximately 1 Gyr younger than the other two brightest galaxies. In addition, this galaxy is fainter by ~0.2 mag in Ks and ~0.15 mag in J, with respect to the other two bright galaxies.

7. Discussion and conclusions

XMMU J1229+0151 is a rich, X-ray luminous galaxy cluster at redshift $z = 0.975$, that benefited from a good multi-wavelength coverage and which represents an excellent laboratory for studying galaxy evolution. The high-quality ACS imaging data combined with the FORS2 spectra allowed us to derived accurate galaxy photometry, and with additional NIR J and Ks data we performed an SED analysis.

Our main conclusions are:

– From the X-ray spectral analysis, we obtained a global cluster temperature of 6.4 keV and a luminosity $L_x[0.5-2.0]$ keV $= 1.3 \times 10^{44}$ erg s^{-1}, indicating that XMM1229 is a massive cluster. Fixing the redshift to the spectroscopic value, we obtain the metal abundance $Z/Z_\odot = 0.34^{+0.14}_{-0.13}$.

– We measured the cluster velocity dispersion σ using the 27 galaxy redshifts obtained with FORS2, $\sigma = 683 \pm 62$ km s^{-1}. The velocity dispersion is below the value expected from the mean $T-\sigma$ relation (Rosati et al. 2002) for

Table 6. Properties of the three brightest galaxies.

ID (1)	z_{850} mag (2)	dist ["] (3)	Mass [10^{11} $M_\odot$] (4)	Age [Gyr] (5)
3025	21.051 ± 0.002	78	$2.0^{+0.6}_{-0.9}$	$4.9^{+0.89}_{-2.36}$
3430	21.055 ± 0.002	5	$2.3^{+0.3}_{-1.1}$	$5.7_{-2.84}$
3507	21.468 ± 0.002	1	$2.6^{+0.3}_{-1.1}$	$5.7_{-2.50}$

the cluster temperature, however it is still consistent with the relation within its large scatter.

– Using the morphological templates of Postman we made a visual classification of the cluster galaxies. We found a predominance of ellipticals (15/21), with only four members classified as S0, one irregular galaxy and one late-type Sb galaxy. In order to investigate whether this apparent absence of S0s and also to propose a means of subsequently populating the faint end of the cluster red-sequence, we constructed a "red-sequence" sample, based on the galaxies morphology, colour, and total magnitude. We find that the fraction of ellipticals in the locus of the red-sequence pertaining to the "red-sequence" galaxy sample, 22/31, is a factor of three higher than the number of S0s in the spectroscopic sample (9/31). Furthermore, there are two pairs of red galaxies in the spectroscopic sample.

– In addition to the visual morphological classification, we fitted Sersic models to the surface brightness profiles of the two galaxy samples. The distribution of the best-fit structural parameters n peaks at 3.9, suggesting a majority of bulge-dominated galaxies. The median effective radius is $0.275''$, approximately the radius chosen for measuring the $i_{775} - z_{850}$ colour ($r = 0.25''$).

– Two methods were explored to measure the scatter of the CMR: (i) in a first approach, which is the standard one presented in the literature, we corrected the different PSFs of the i_{775} and z_{850} bands to measure accurate galaxy aperture magnitudes; and (ii) in an alternative approach, we used the best-fit galaxy model magnitudes obtained by fitting the surface brightness profiles. The CMR at this high redshift is found already to be very tight, with an intrinsic scatter of 0.04 mag when considering only the passive members, a spread similar to that of the local clusters, confirming that the cluster ETGs assembled early and on short timescales. The scatter in the red-sequence is similar for these two independent methods, showing that the second method is robust against uncertainties in PSF corrections. The slope of the red-sequence including only the cluster members is -0.031 ± 0.016, and slightly decreases to -0.022 ± 0.008 when accounting also for the "red-sequence" galaxies.

These results agree with conclusions drawn for the ACS Intermediate Redshift Cluster Survey (see e.g., Mei et al. 2006; Blakeslee et al. 2003a; Mei et al. 2009), where no significant redshift evolution was found in the CMR scatter and slope. We note that in the referred papers, galaxy colours were measured in apertures of variable size corresponding to the effective radius.

– The spectrophotometric analysis shows a red-sequence populated by moderately massive galaxies, with a median stellar mass of 7.4×10^{10} $M_\odot$. The combined SED + spectral fit to the stacked spectrum of the passive members allowed us to constrain the ages of the ETGs to be $3.7^{+0.4}_{-0.5}$ Gyr, corresponding to a formation redshift $z_f = 3.0 \pm 0.5$, similar to that of other $z \sim 1$ clusters (e.g., Gobat et al. 2008).

– The inferred star-formation histories imply that the cluster galaxies have completed most of the chemical enrichment, which is consistent with the high metal abundance of the ICM, $Z \sim 1/3 \, Z_\odot$, as derived from our X-ray analysis (see Table 2).

– As widely reported in the literature, we found a clear signature of significant *downsizing*, since the correlation between stellar mass and galaxy age favours an anti-hierarchical behaviour where the most massive galaxies are the oldest, and tend to be the closest to the cluster core (Figs. 11, 12).

References

Appenzeller, I., Fricke, K., Fürtig, W., et al. 1998, The Messenger, 94, 1
Anders, E., & Grevesse, N. 1989, Geochim. Cosmochim. Acta, 53, 197
Arnaud, K. A. 1996, Astronomical Data Analysis Software and Systems V, 101, 17
Arnaud, M., Neumann, D. M., Aghanim, N., et al. 2001, A&A, 365, L80
Arnaud, M., Pointecouteau, E., & Pratt, G. W. 2005, A&A, 441, 893
Baldry, I. K., Glazebrook, K., Brinkmann, J., et al. 2004, ApJ, 600, 681
Beers, T. C., Flynn, K., & Gebhardt, K. 1990, AJ, 100, 32
Bertin, E., & Arnouts, S. 1996, A&AS, 117, 393
Biviano, A., Katgert, P., Thomas, T., & Adami, C. 2002, A&A, 387, 8
Blakeslee, J. P., Franx, M., Postman, M., et al. 2003a, ApJ, 596, L143
Blakeslee, J. P., Anderson, K. R., Meurer, G. R., Benítez, N., & Magee, D. 2003b, in Astronomical Data Analysis Software and Systems XII, ed. G. Piotto, G. Meylan, S. G. Djorgovski, & M. Riello (San Francisco: ASP), ASP Conf. Ser., 295, 257
Blakeslee, J. P., Holden, B. P., Franx, M., et al. 2006, ApJ, 644, 30
Blanton, M. R., Eisenstein, D., Hogg, D. W., Schlegel, D. J., & Brinkmann, J. 2005, ApJ, 629, 143
Böhringer, H., Mullis, C., Rosati, P., et al. 2005, The Messenger, 120, 33
Bower, R. G., Lucey, J. R., & Ellis, R. S. 1992, MNRAS, 254, 589
Bower, R. G., Benson, A. J., Malbon, R., et al. 2006, MNRAS, 370, 645
Bruzual, G., & Charlot, S. 2003, MNRAS, 344, 1000
Chabrier, G. 2003, PASP, 115, 763
Cavaliere, A., & Fusco-Femiano, R. 1976, A&A, 49, 137
Cowie, L. L., Songaila, A., Hu, E. M., & Cohen, J. G. 1996, AJ, 112, 839
Croton, D. J., Springel, V., White, S. D. M., et al. 2006, MNRAS, 365, 11
Danese, L., de Zotti, G., & di Tullio, G. 1980, A&A, 82, 322
Dawson, K., et al. 2009, in prep.
De Lucia, G., & Blaizot, J. 2007, MNRAS, 375, 2

De Lucia, G., Kauffmann, G., & White, S. D. M. 2004, MNRAS, 349, 1101
De Lucia, G., Springel, V., White, S. D. M., Croton, D., & Kauffmann, G. 2006, MNRAS, 366, 499
de Vaucouleurs, G. 1961, ApJS, 5, 233
Demarco, R., Rosati, P., Lidman, C., et al. 2005, A&A, 432, 381
Demarco, R., Rosati, P., Lidman, C., et al. 2007, ApJ, 663, 164
de Propris, R., Eisenhardt, P. R., Stanford, S. A., & Dickinson, M. 1998, ApJ, 503, L45
Dressler, A., Smail, I., Poggianti, B. M., et al. 1999, ApJS, 122, 51
Dickey, J. M., & Lockman, F. J. 1990, ARA&A, 28, 215
Eggen, O. J., Lynden-Bell, D., & Sandage, A. R. 1962, ApJ, 136, 748
Fassbender, R. 2008, arXiv e-prints, 806
Gladders, M. D., & Yee, H. K. C. 2000, AJ, 120, 2148
Gobat, R., Rosati, P., Strazzullo, V., et al. 2008, A&A, 488, 853
Hilton, M., Collins, C. A., Stanford, S. A., et al. 2007, ApJ, 670, 1000
Holden, B. P., Blakeslee, J. P., Postman, M., et al. 2005, ApJ, 626, 809
Homeier, N. L., Demarco, R., Rosati, P., et al. 2005, ApJ, 621, 651
Kaastra, J. 1992, in Internal SRON-Leiden Report, updated version 2.0
Kauffmann, G., & Charlot, S. 1998, MNRAS, 294, 705
Kodama, T., Yamada, T., Akiyama, M., et al. 2004, MNRAS, 350, 1005
Kroupa, P., & Weidner, C. 2003, ApJ, 598, 1076
Larson, R. B. 1974, MNRAS, 166, 585
Lidman, C., Rosati, P., Demarco, R., et al. 2004, A&A, 416, 829
Lidman, C., Rosati, P., Tanaka, M., et al. 2008, A&A, 489, 981
Liedahl, D. A., Osterheld, A. L., & Goldstein, W. H. 1995, ApJ, 438, L115
Maraston, C. 2005, MNRAS, 362, 799
Mei, S., Holden, B. P., Blakeslee, J. P., et al. 2006, ApJ, 644, 759
Mei, S., Blakeslee, J. P., Côté, P., et al. 2007, ApJ, 655, 144
Mei, S., Holden, B. P., Blakeslee, J. P., et al. 2009, ApJ, 690, 42
Menci, N., Fontana, A., Giallongo, E., Grazian, A., & Salimbeni, S. 2006, ApJ, 647, 753
Menci, N., Rosati, P., Gobat, R., et al. 2008, ApJ, 685, 863
Moorwood, A., Cuby, J.-G., & Lidman, C. 1998, The Messenger, 91, 9
Persson, S. E., Murphy, D. C., Krzeminski, W., Roth, M., & Rieke, M. J. 1998, AJ, 116, 2475
Postman, M., Franx, M., Cross, N. J. G., et al. 2005, ApJ, 623, 721
Press, W. H., & Schechter, P. 1974, ApJ, 187, 425
Rosati, P., Borgani, S., & Norman, C. 2002, ARA&A, 40, 539
Rosati, P., et al. 2009, in preparation
Salpeter, E. E. 1955, ApJ, 121, 161
Sandage, A., & Visvanathan, N. 1978, ApJ, 225, 742
Scodeggio, M. 2001, AJ, 121, 2413
Schlegel, D. J., Finkbeiner, D. P., & Davis, M. 1998, ApJ, 500, 525
Sersic, J. L. 1968, Cordoba, Argentina, Observatorio Astronomico
Simard, L., Willmer, C. N. A., Vogt, N. P., et al. 2002, ApJS, 142, 1
Sirianni, M., Jee, M. J., Benítez, N., et al. 2005, PASP, 117, 1049
Somerville, R. S., Hopkins, P. F., Cox, T. J., Robertson, B. E., & Hernquist, L. 2008, MNRAS, 391, 481
Stanford, S. A., Romer, A. K., Sabirli, K., et al. 2006, ApJ, 646, L13
Thomas, D., Maraston, C., Bender, R., & Mendes de Oliveira, C. 2005, ApJ, 621, 673
Toomre, A. 1977, Evolution of Galaxies and Stellar Populations, 401
van der Wel, A., Franx, M., van Dokkum, P. G., et al. 2005, ApJ, 631, 145
van Dokkum, P. G. 2005, AJ, 130, 2647
Vandame, B. 2004, Ph.D. Thesis, Nice University, France
Visvanathan, N., & Sandage, A. 1977, ApJ, 216, 214
White, S. D. M., & Rees, M. J. 1978, MNRAS, 183, 341
Wilms, J., Allen, A., & McCray, R. 2000, ApJ, 542, 914
Wu, X.-P., Xue, Y.-J., & Fang, L.-Z. 1999, ApJ, 524, 22